Journal of Colloid and Interface Science 697 (2025) 137955

Contents lists available at ScienceDirect

Journal of Colloid And Interface Science

journal homepage: www.elsevier.com/locate/jcis

Regular Article

Investigation of Cu-doped MnCeOx in PTFE catalytic fiber for synergistic removal of CB and NO at low temperature

Shengyong Lu [a,b], Xuanhao Guo [a,b], Manting Chen [c], Guanjie Wang [b], Juan Qiu [a,b], Jiaming Ding [a,b], Minghui Tang [a], Zhengdong Han [b], Yaqi Peng [a,*], Jianhua Yan [a]

[a] State Key Laboratory of Clean Energy Utilization, Institute for Thermal Power Engineering, Zhejiang University, Hangzhou 310027, China
[b] Taizhou Institute of Zhejiang University, Zhejiang University, Taizhou 318000, China
[c] Taizhou Pollution Control Technology Center Co., Ltd, Taizhou University, Taizhou 318000, China

HIGHLIGHTS

- MnCeOx derived from MOFs were effective for the synergistic removal CB and NO.
- Cu doping improved the activity of catalysts by inhibiting the formation of NH_4Cl.
- Catalytic PTFE fibers were prepared by membrane crack method.
- Catalytic PTFE fibers showed excellent removal efficiency of dioxins.
- Catalytic PTFE fibers have a certain adsorption effect on dioxin and SO_2.

GRAPHICAL ABSTRACT

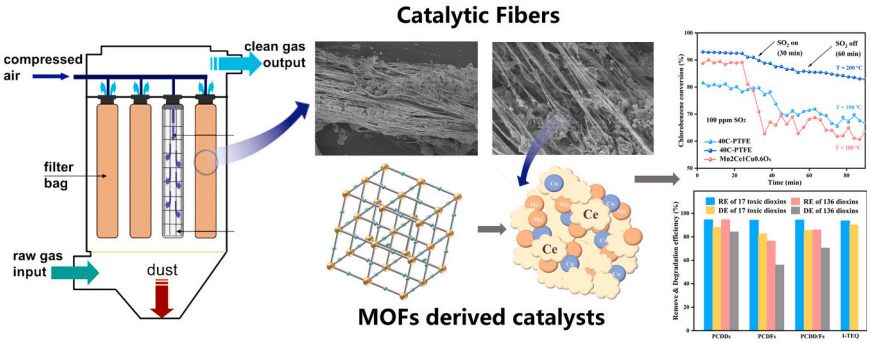

ARTICLE INFO

Keywords:
Dioxin
Synergistic removal mechanism
MOFs
PTFE catalytic fibers

ABSTRACT

The synergistic removal of multiple pollutants from flue gas has attracted growing interest in recent years. In this study, Cu-doped $MnCeO_x$ catalysts were synthesized via an impregnation method and integrated into PTFE fibers using a split-film process to enable the simultaneous removal of chlorobenzene (CB) and nitrogen oxide (NO). Among the catalysts tested, $Mn_2Ce_1Cu_{0.6}O_x$ exhibited the highest performance, achieving 90 % CB degradation and 100 % NO conversion at 180 °C. The PTFE-based catalytic fibers also demonstrated excellent removal efficiency, reaching 83.7 % for dioxins at the same temperature. A possible reaction mechanism is proposed in which the NH_3-SCR process facilitates CB oxidation by generating reactive intermediates. Cu doping was found to enhance the density of acid sites and promote the ring-opening of CB, thereby suppressing chlorine accumulation and improving catalyst stability. These findings provide valuable insights for the development and optimization of catalytic bag filters for the efficient, synergistic removal of multiple pollutants from industrial emissions.

* Corresponding author.
E-mail address: pengyaqi@zju.edu.cn (Y. Peng).

https://doi.org/10.1016/j.jcis.2025.137955
Received 17 March 2025; Received in revised form 14 May 2025; Accepted 20 May 2025
Available online 20 May 2025

1. Introduction

Incineration has become the predominant method for municipal solid waste treatment in China; however, the resulting flue gas typically contains a range of pollutants, including particulate matter (PM), nitrogen oxides (NO_x), and dioxins [1]. Strict environmental regulations have been implemented to control the emissions of dioxins and NO_x in flue gas. To address this issue, catalytic oxidation technology is commonly employed for the removal of gaseous pollutants, owing to its advantages of high efficiency and low energy consumption [2,3], by applying bag filter to remove particulates. In recent years, considerable research has focused on the development of catalytic bag filters for the simultaneous control of multiple pollutants, enabling the synergistic removal of both gaseous contaminants and particulate matter [4,5].

A catalytic bag filter integrates catalytic and filtration functions by incorporating catalysts directly onto the filter material [6]. Common preparation methods include impregnation method and the redox method. Jiang et al. prepared a polytetrafluoroethylene (PTFE) catalytic bag filter by impregnation method with La modified manganese oxide catalyst [7]. The filter achieved approximately 90 % NO_x conversion efficiency at 200 °C and demonstrated good resistance to H_2O and SO_2. However, the surface-loaded catalysts were prone to detachment during pulse cleaning, which limited the long-term stability of the system in practical applications. Luo et al. prepared an efficient catalytic membrane used for laminating with bag filter [8]. Flowerlike $Mn_yFe_zO_x$ amorphous oxide catalysts were anchored into the membrane via redox method. The NO removal efficiency of catalytic membrane was higher than 90 % at 115–180 °C under a GHSV of 74,000 mL $g^{-1}h^{-1}$. However, the redox method suffers from low efficiency, making it unsuitable for industrial application, as it typically requires over 12 h to produce a single batch of catalytic filter materials, with production capacity fundamentally constrained by the volume of the reaction reactors [9]. Compared with other methods, the split film process is considered the most promising approach due to its advantages, including a simple preparation procedure and strong catalyst retention. For example, Jin et al. successfully prepared catalyst-embedded PTFE fibers using the split film process, achieving uniform dispersion of the catalyst both on the surface and within the interior of the fibers [10]. However, approximately 43–50 % of the catalysts incorporated into the PTFE fibers were embedded too deeply, limiting their exposure and reducing their effectiveness in the catalytic reaction. Therefore, it is crucial to design catalysts with high intrinsic activity and optimal surface accessibility to fully realize the potential of catalytic bag filters.

Metal-organic framework materials (MOFs) has been widely used in various fields, including hydrogen storage [11], gas sensors [12], supercapacitors [13], adsorption [14], and photocatalysis [15]. Catalytic oxidation [16] was also explored, as catalysts derived from MOFs inherit the advantages of MOF materials, such as tunable structures, high specific surface area, and abundant porosity. The self-assembly of metal ions and organic ligands provides excellent precursor templates for catalysts, making them highly suitable for heterogeneous catalysis. Self-assembly of metal ions and organic ligands provided catalyst excellent precursor templates, which were highly suitable for heterogeneous catalysis [17]. Chai et al. prepared a series of V_2O_5/TiO_2 catalysts via wet impregnation over MIL-125(Ti) support, followed by calcination [18]. Among them, the 0.8VTi sample achieved 100 % chlorobenzene (CB) conversion at 250 °C. Jiang et al. systhesized MnO_x materials using various Mn-based MOFs as templates for CB catalytic oxidation [19]. They found that the precursors significantly influenced the structural morphology of the resulting MnOx materials. MnO_2 derived from Mn-MOF-74 in the presence of H_2O_2 exhibited the best catalytic activity, with a T_{90} of 174 °C. This green and economical preparation method offers a promising strategy for designing efficient catalysts.

Another approach to enhance the activity of the catalyst is metal doping. It was reported that Cu doping could boost the catalytic activity of manganese oxide catalyst by facilitating the electron transfer between CuO and MnO, due to the strong synergistic effect exists between Cu and Mn [20–22]. Liu et al. found that Cu-Mn-BTC (Trimesic acid) contained more Lewis acid sites than Mn-BTC because Cu doping increased the concentration of Lewis acid sites on the catalytic surface [23]. Shen et al. prepared Cu-doped $SmMn_2O_5$ mullite catalysts and found that Cu doping created Cu^{2+}-O-Mn^{4+} active composite sites [24]. Cu-doped $SmMn_2O_5$ mullite catalysts exhibited 90 % conversion of toluene at 206 ℃ and displayed robust stability with the presence of water.

In this study, MnCe-BTC, synthesized via a simple solvothermal reaction, was selected as the template, and copper was doped by impregnation. The $Mn_2Ce_1Cu_{0.6}O_x$ catalyst, which exhibited the best catalytic performance, was then mixed with PTFE resin, compressed, rolled, stretched, and slitted to prepare catalytic fibers. Chlorobenzene and NO were selected as model pollutants to study the synergistic removal of dioxins and NO_x. The physicochemical properties of the catalysts and catalytic fibers were characterized to assess the impact of Cu doping. Using in situ DRIFTS data, the potential catalytic mechanisms for the synergistic removal of CB and NO were further explored.

2. Materials and methods

2.1. Synthesis of the catalysts and the catalytic PTFE fibers

Using a typical solvothermal method, 0.502 g manganous nitrate tetrahydrated ($Mn(NO_3)_2{\cdot}4H_2O$), 0.434 g cerium nitrate hexahydrate ($Ce(NO_3)_3{\cdot}6H_2O$) and 0.567 g trimesic acid (BTC) were fully dissolved in 60 mL *N*,*N*-Dimethylformamide (DMF). The solution was then transferred to a PTFE hydrothermal reactor and heated at 120 °C for 24 h to obtain MnCe-BTC precursor. The precursor was calcined at 300 °C for 2 h under air atmosphere to obtain $Mn_2Ce_1O_x$ (molar ratio) catalyst as shown in Fig. 1a. Using a typical impregnation method, the obtained MnCe-BTC precursor and cupric nitrate ($Cu(NO_3)_2$) with different molar ratios were weighted and dissolved in the deionized water. The solution aforementioned was magnetically stirred at room temperature at 200 rpm for 2 h and then was dried overnight to obtain blue particles. $Mn_2Ce_1Cu_{0.2}O_x$, $Mn_2Ce_1Cu_{0.6}O_x$, $Mn_2Ce_1Cu_1O_x$ were prepared after calcination at 300 °C for 2 h under air atmosphere as shown in Fig. 1b. All reagents and solutions mentioned above were purchased from Aladdin and are of analytical reagent (AR) grade.

The catalytic PTFE fibers were prepared by split film process as shown in Fig. 1c. The $Mn_2Ce_1Cu_{0.6}O_x$ catalyst powder was added to PTFE resin and rolled to mix well. White oil (30 wt% of total weight) was then added as lubricant and dried at 60 °C overnight. The catalyst was evenly coated in the resin along with the lubricating oil. The mixture was extruded into thin rod with a diameter of 3 cm and then rolled into a film. The prepared film was sent to degreasing machine and heated at 120 °C to eliminate white oil. After degreasing, the film was heated and stretched at 350 °C and fed into a pair of needle rollers to break the film to form catalytic fibers named as C-PTFE. A series of C-PTFE were prepared by changing the mass ratios of $Mn_2Ce_1Cu_{0.6}O_x$, including 20C-PTFE, 30C-PTFE, and 40C-PTFE corresponding to 2:8, 3:7 and 4:6 (catalysts: PTFE), respectively.

2.2. Catalysts characterization

The catalysts and PTFE catalytic fibers were characterized by various techniques including scanning electron microscopy (SEM), transmission electron microscopy (TEM), element mapping (EDS), X-ray diffractometer (XRD), N_2 adsorption–desorption, X-ray photoelectron spectroscopic (XPS), temperature programmed H_2 reduction (H_2-TPR), temperature programmed O_2 desorption (O_2-TPD), temperature programmed NH_3 desorption (NH_3-TPD), Pyridine infrared (Py-IR), thermogravimetric (TG), in situ diffuse reflectance infrared Fourier transform spectroscopy (in situ DRIFTS). Mechanical properties of fibers were tested using monofilament strength meter and the contact angles of

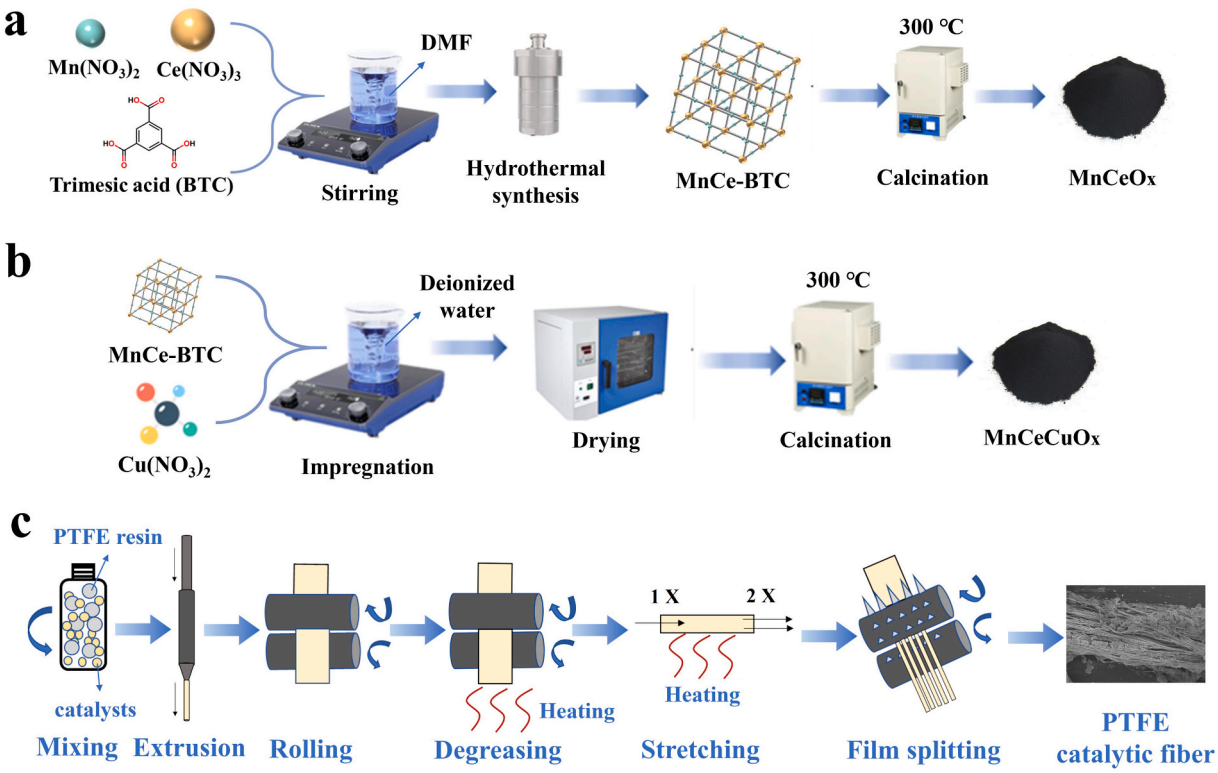

Fig. 1. Schematic diagram of (a) $Mn_2Ce_1O_x$ catalysts preparation; (b) $MnCeCuO_x$ catalysts preparation; (c) cataytic fibers preparation.

the liquid were measured by the seat drop method. More details of the characterization experiments were provided in the Supporting materials.

2.3. Catalytic activity evaluation

The catalytic performance of samples was evaluated in a fixed bed flow continuous reactor (Fig. S1) under atmospheric pressure. The sample (weight: 200 mg, particle size: 40–60 mesh) was placed within a quartz reactor (i. d. = 8 mm) and securely positioned using quartz wool at both ends of the catalyst. The flow rate was precisely adjusted by mass flow controllers (MFCs) maintaining 100 ppm CB, 500 ppm NO, 500 ppm NH_3, 11 % vol O_2 and N_2 as balance. The space velocity was 30,000 mL g^{-1} h^{-1} and the reaction time was 30 min at each temperature. The concentration of CB was continuously monitored using an online gas chromatography system (GC, Fuli GC-9790 plus), equipped with a thermal conductivity detector (TCD) and two flame ionization detectors (FID). The concentrations of NOx were detected by flue gas analyzer (Gasboard-3000plus, Ruiyi). The conversion efficiency of CB and NO were calculated with the following formulas:

$$\eta_{CB} = \frac{C_{CB}^{in} - C_{CB}^{out}}{C_{CB}^{in}} \times 100\%$$

$$\eta_{NO} = \frac{C_{NO-}^{in} C_{NO}^{out}}{C_{NO}^{in}} \times 100\%$$

where η_{CB} and η_{NO} represented the conversion efficiency of CB and NO, respectively. C_{CB}^{in} and C_{NO}^{in} represented the inlet concentration of CB and NO, respectively. C_{CB}^{out} and C_{NO}^{out} represented the outlet concentration of CB and NO, respectively. More details of catalytic activity evaluation divices and dioxins experimental parameters were provided in the Supporting materials.

3. Results and discussion

3.1. Catalytic activity

Fig. 2a and Fig. 2b illustrated the conversion rate of catalysts when used for the synergistic removal of CB and NO. For CB, the catalytic activities of $Mn_2Ce_1Cu_{0.6}O_x$ (T_{90} = 180.9 °C) and $Mn_2Ce_1Cu_{0.2}O_x$ (T_{90} = 186.1 °C) were higher than that of $Mn_2Ce_1O_x$ (T_{90} = 195.2 °C), indicating that Cu doping significantly enhanced the catalytic activity of catalysts. However, too much Cu species showed adverse effect and caused a decline in $Mn_2Ce_1Cu_1O_x$ (T_{90} = 202.7 °C). Combined with SEM image analysis (Fig. 3d), it was possible that excessive Cu species would react with O_2 to form CuO coating layer on the surface of catalyst, covering the active sites and obstructing electron transfer. All catalysts showed excellent NO catalytic activity that NO conversion rates were all higher than 90 % at 140 °C. However, higher temperature seemed to limit the NH_3-SCR reaction, resulting in a decrease of NO conversion rate [25]. $Mn_2Ce_1Cu_{0.6}O_x$ exhibited the highest low-temperature catalytic activity, reaching 90 % CB conversion rate and 100 % NO conversion rate at 180 °C. Fig. 2c and d illustrated the conversion rate of CB and NO for the PTFE catalytic fibers, respectively. Compared to the catalyst powder, the catalytic activity of catalytic fibers was slightly lower, which may be attributed to a portion of the catalysts being encapsulated within the fibers, thereby limiting its exposure and participation in the reaction. For CB, the catalytic activity of 40C-PTFE (T_{90} = 185.4 °C) was much higher than that of 20C-PTFE (T_{90} = 223.2 °C), indicating that the higher catalyst content improved the catalytic performance. On the other hand, 30C-PTFE (T_{90} = 192.8 °C) exhibited a T_{90} value close to that of 20C-PTFE, suggesting that the influence of catalysts loading on activity was limited. Notably, 40C-PTFE demonstrated a broad operating temperature window for NO, maintaining a conversion rate above 90 % across a temperature range of 130 °C to 220 °C. $Mn_2Ce_1Cu_{0.6}O_x$ demonstrated good stability at 250 °C, as shown in Fig. 2e. The deactivation of the catalysts occurred after 4 h, with the conversion rate of CB dropping from 100 % to 70 % and then remaining steady. In the 24 h

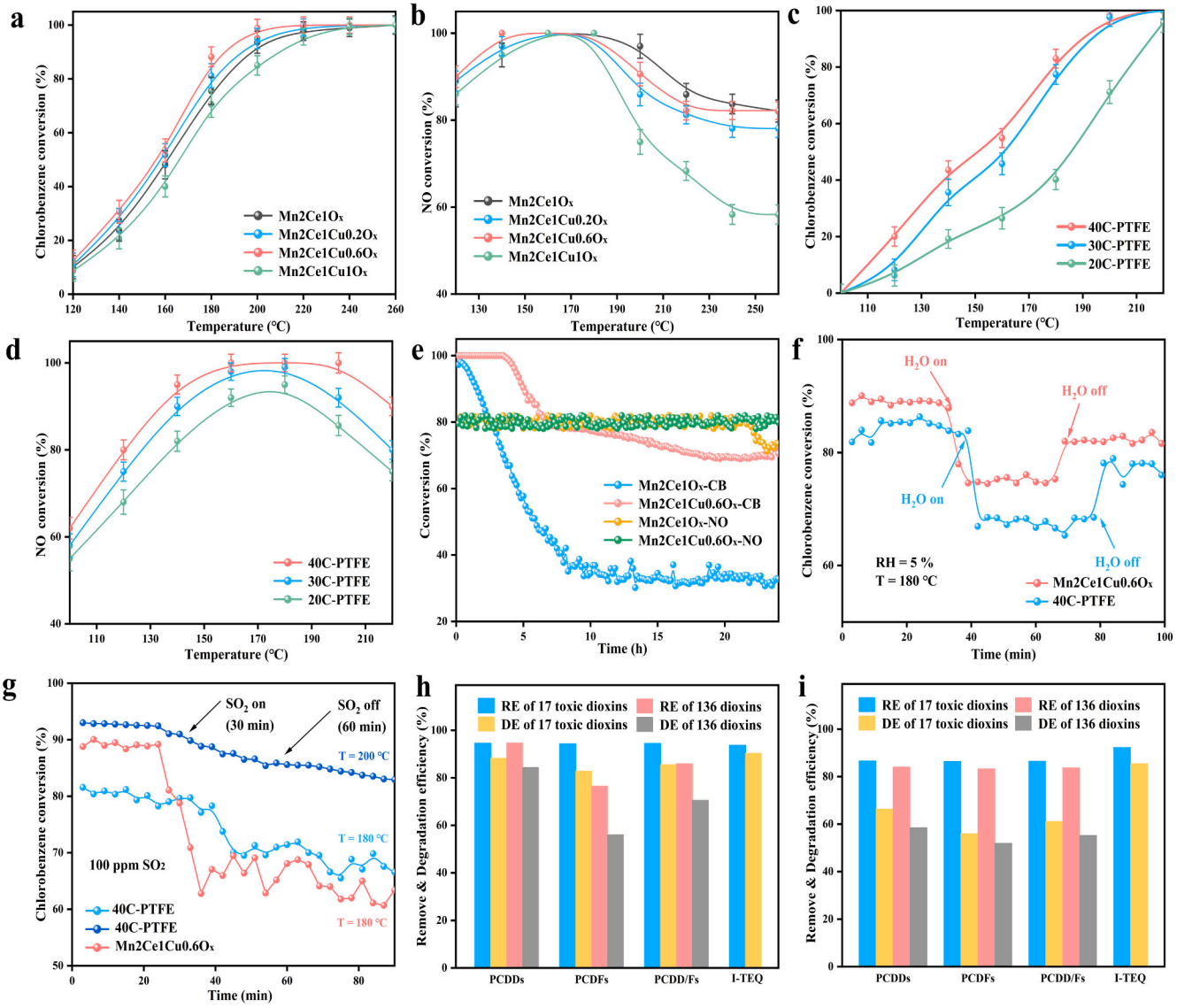

Fig. 2. CB conversion of (a) catalysts and (c) catalytic fibers; NO conversion of (b) catalysts and (d) catalytic fibers; (e) stability tests; (f) H_2O resistances; (g) SO_2 resistances; dioxins remove and degradation efficiency of (h) catalysts and (i) catalytic fibers.

stability test, the conversion rate of NO maintained 80 % for about 22 h before declining slightly to 76 %. In comparison, Mn_2Ce_1Ox showed significantly lower stability, with the CB conversion dropping from 100 % to 35 % within 10 h. These results confirm that Cu-doping greatly enhanced the long-term stability of catalysts.

The effect of water vapor on the catalytic activity was evaluated by introducing water vapor into the reaction system, adjusting the relative humidity to around 5 % at 180 °C. As shown in Fig. 2f, the conversion rate of CB decreased by about 15 % for $Mn_2Ce_1Cu_{0.6}O_x$ and 20 % for 40C-PTFE. However, after the water vapor introduction ceased, the conversion rates could increase approximately 5 % and 8 %, respectively. The effect of SO_2 on the catalytic activity was evaluated by introducing 100 ppm SO_2 into the reaction system at 180 °C (Fig. 2g). The degradation rate of CB over $Mn_2Ce_1Cu_{0.6}O_x$ rapidly decreased by about 20 % and slowly decreased to about 60 % despite SO_2 was off. Surprisingly, the deactivation rate of 40C-PTFE was significantly lower than that of $Mn_2Ce_1Cu_{0.6}O_x$. Increasing the temperature to 200 °C further reduced the deactivation of 40C-PTFE, suggesting that this phenomenon is linked to adsorption ehavior, specifically the reduced adsorption of SO_2 at higher temperatures. Generally, SO_2 competes with CB and NO for active sites, leading to the formation of metal sulfate and causing irreversible catalyst deactivation [26]. However, the fiber network structure and porous membrane of C-PTFE provided additional adsorption sites for SO_2 and reduced the competitive adsorption [7,27]. Therefore, 40C-PTFE showed better SO_2 resistance than $Mn_2Ce_1Cu_{0.6}O_x$.

Furthermore, the catalytic activity of $Mn_2Ce_1Cu_{0.6}O_x$ for dioxin removal was evaluated, and the results are shown in Fig. 2h. At 180 °C, 86.0 % of the dioxins were effectively removed. Among them, 94.4 % toxic dioxins were effectively removed and 85.5 % were degraded. The remove and degradation efficiency of I-TEQ were 93.6 % and 90.3 %, respectively. The remove efficiency of PCDDs (94.5 %) was higher than that of PCDFs (94.2 %) as PCDFs contained more high-chlorinated homologues, which were more stable and were harder to degrade than low-chlorinated homologues [28]. The catalytic activity of 40C-PTFE was lower than that of $Mn_2Ce_1Cu_{0.6}O_x$ as shown in Fig. 2i, which was consistent with the CB and NO test results. When C-PTFE were used for tests, 83.7 % dioxins were effectively removed at 180 °C. Among them, 86.5 % toxic homologues were effectively removed and 61.1 % were degraded. The remove efficiency and degradation efficiency of I-TEQ were 92.3 % and 85.5 %, respectively. Compared to catalysts powder, 40C-PTFE adsorbed more dioxins indicating that PTFE fiber has a certain adsorption effect on dioxins which was consistent with SO_2 test results.

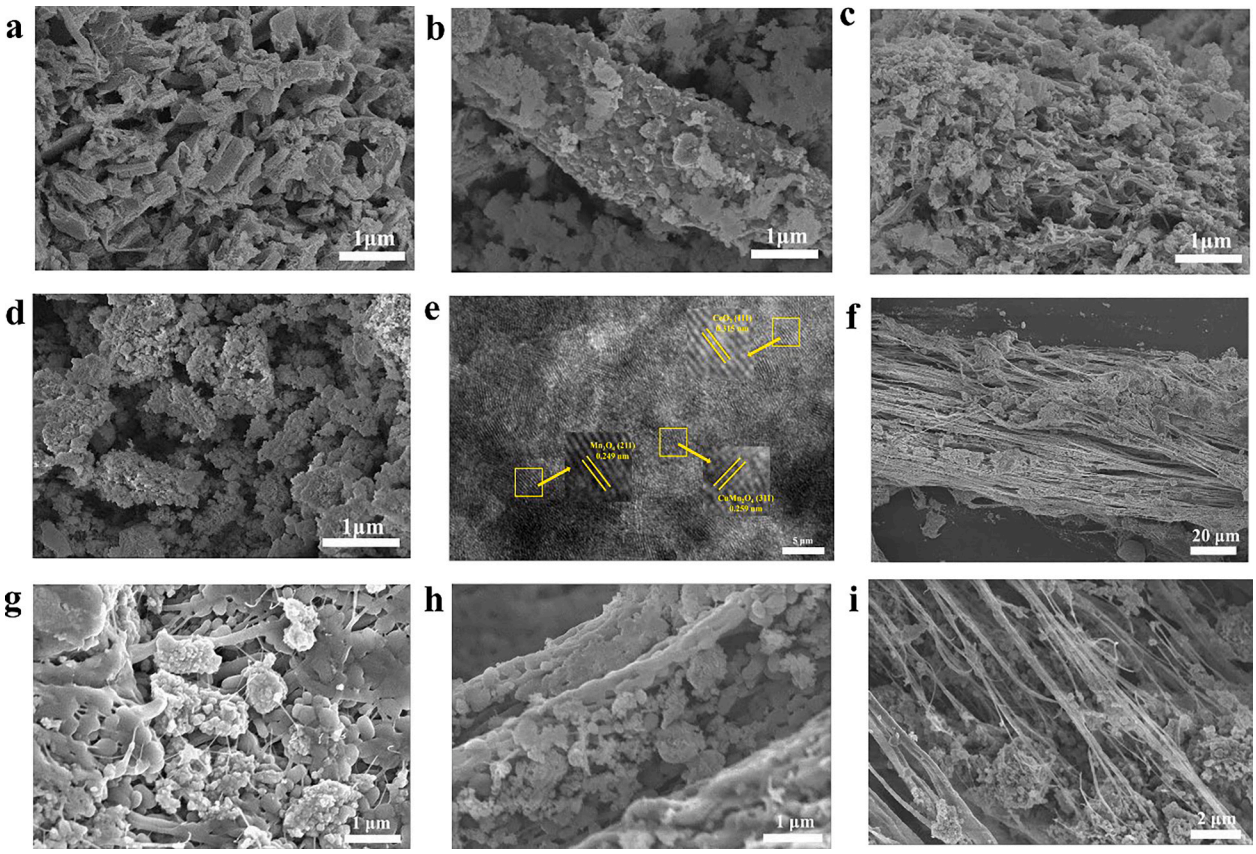

Fig. 3. SEM images of (a) $Mn_2Ce_1O_x$; (b) $Mn_2Ce_1Cu_{0.2}O_x$; (c) $Mn_2Ce_1Cu_{0.6}O_x$; (d) $Mn_2Ce_1Cu_1O_x$; TEM images of (e) $Mn_2Ce_1Cu_{0.6}O_x$; SEM images of (f) 40C-PTFE fibers; (g) 20C-PTFE; (h) 30C-PTFE; (i) 40C-PTFE.

The distributions of PCDD/Fs homologues were illustrated in Figs. S3 and S4. The behavior of $Mn_2Ce_1Cu_{0.6}O_x$ and 40C-PTFE were similar that the removal efficiency of high-chlorinated homologues was lower than that of low-chlorinated homologues, especially HxCDD/Fs. Some PeCDFs were generated during the degradation process, indicating that high-chlorinated homologues underwent dechlorination, resulting in the formation of low-chlorinated homologues.

3.2. Morphology

The morphology of $MnCeCuO_x$ with different Cu content were shown in Fig. 3a–d. All catalysts exhibited rod-like structure, which was reported to exhibit superior catalytic activity for pollutants compared to cubic and octahedra-shape [29]. And the large aspect ratio and anisotropy one-dimensional structure of nano rods provided catalyst with abundant active sites and directional paths for electron transport [30]. Tiny particles appeared on the surface of $Mn_2Ce_1Cu_{0.2}O_x$ could be regarded as Cu species. $Mn_2Ce_1Cu_{0.6}O_x$ showed longer and thinner rod-like structure with porous structures appearing, which was conducive to gas diffusion and adsorption. Further increasing the Cu content led to the formation of CuO coating layer on the surface of $Mn_2Ce_1Cu_1O_x$, which obstructed the catalytic reactions [31]. EDS-mapping was also employed to further study the element distribution of $Mn_2Ce_1Cu_{0.6}O_x$ as shown in Fig. S5. It was found that Ce, Mn and Cu were uniformly distributed. The lattice spacing of 0.315, 0.249 and 0.259 nm were displayed in Fig. 3e, corresponding to the crystal face of CeO_2 (111), Mn_3O_4 (211) and $CuMn_2O_4$ (311), respectively. The formation of $CuMn_2O_4$ proved the intense interplay between Mn and Cu.

The morphology of C-PTFE with different catalyst content were shown in Fig. 3f–i. The surface of catalytic fibers was covered with cracks caused by the stretching of PTFE film (Fig. 3f). These cracks provided loading sites for catalyst powder and increased the specific surface area of C-PTFE. By the increasing of catalyst content, C-PTFE became thinner and more cracks appeared on the surface of fibers. It was observed that the filaments intertwined with each other to obtain a complex fiber network structure (Fig. 3i). When the catalyst particle size exceeded the fiber diameter, C-PTFE tended to form a fiber network that trapped the catalyst particles on the surface rather than encapsulating them within the fibers. The transformation of loading mode improved the catalytic performance by increasing the exposure of active sites to pollutants. Therefore, a possible forming mechanism of C-PTFE could be proposed. During the stretching process of the PTFE film, the fiber was continuously pulled from the folded wafer, becoming longer and thinner to form node-fiber structures. At low catalyst content, the fiber diameter exceeded the catalyst particle size, causing the catalyst particles to become embedded within the fibers, which led to catalyst deactivation. In contrast, at higher catalyst loading, the increased weight of the catalyst exerted a vertical tensile force, causing premature fiber breakage. This resulted in the formation of numerous filaments that intertwined to create network structures, effectively trapping the catalyst powder, which enhanced contact between the catalysts and contaminants.

3.3. Structural characteristics

The XRD patterns (Fig. 4a) showed that $MnCeCuO_x$ catalysts exhibited diffraction peaks corresponding to $CuMn_2O_4$ (PDF # 74-2422), which indicated the successful formation of Cu-Mn solid solution [31]. Notably, the peak at 35.8°, assigned to the (311) planes of $CuMn_2O_4$, represented the most intense diffraction peak of spinel structure [32]. With the increase of Cu content, the intensity of the 35.8° diffraction peak became more pronounced, and the peak at 28.5°

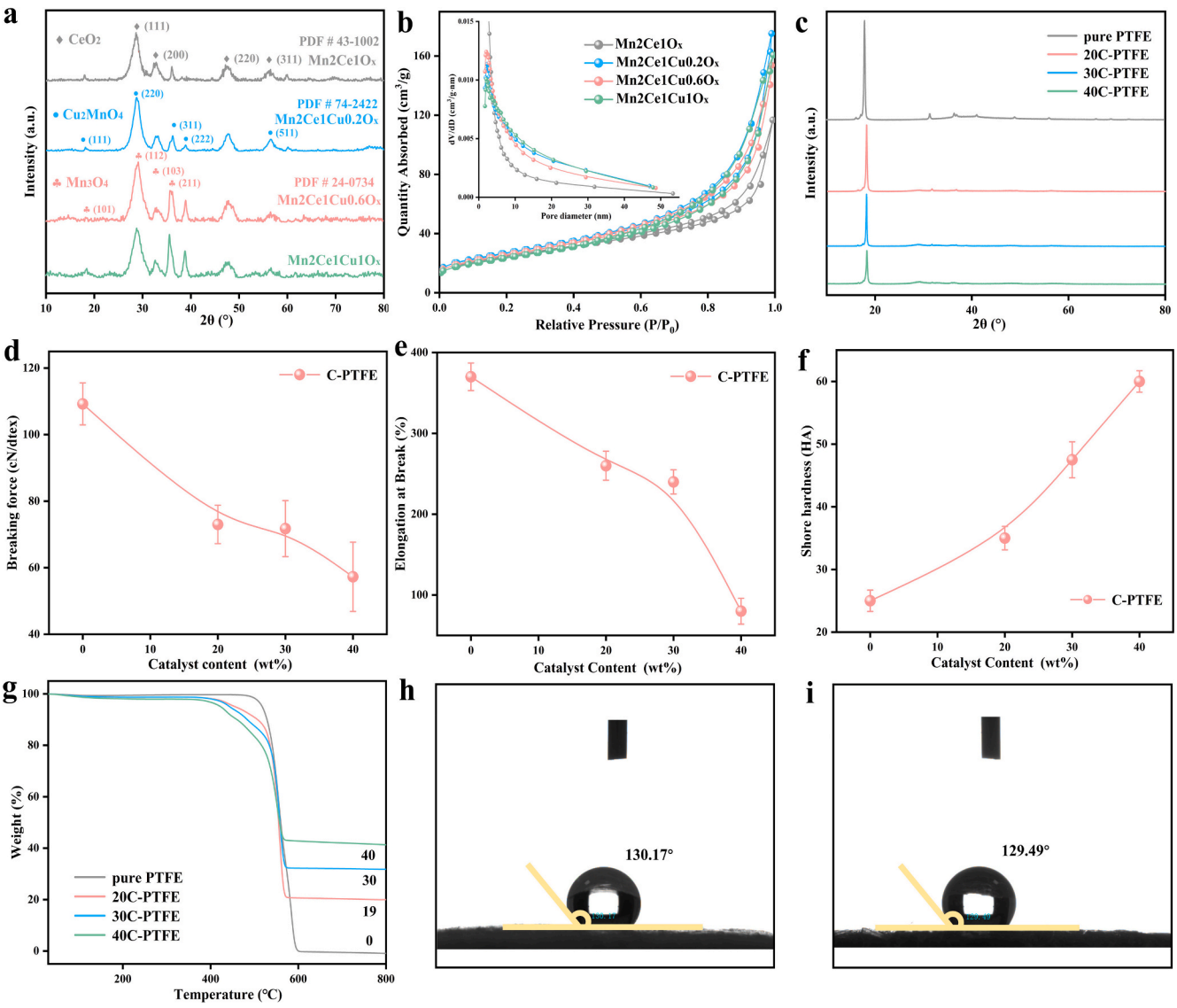

Fig. 4. The XRD patterns (a), N_2 adsorption–desorption isotherm and pore size distribution (b) of catalysts; the XRD patterns (c), breaking force (d), elongation at break (e), shore hardness (f), thermogravimetric analysis (g), water contact angle (i) of catalytic fibers; water contact angle (h) of pure PTFE fibers.

exhibited a slight shift to a higher value. These observations further confirmed the incorporation of Cu into the Mn oxide lattice and the formation of Cu-Mn solid solutions. The pore structure parameters of catalysts were tested and shown in Fig. 4b and Table. S3. All catalysts exhibited type IV adsorption–desorption isotherms with H_3-type hysteresis loops, indicating that the prepared catalysts were typical mesoporous materials. The specific surface area of catalyst exceeded 100 m^2/g, which were mainly attributed to the pyrolysis of MOFs precursor and the generation of structural defects [33]. As the Cu content increased, the specific surface area and pore volume initially rose, followed by a decline. Combined with SEM results, this suggests that excessive Cu species blocked the pores by forming CuO. Among all samples, $Mn_2Ce_1Cu_{0.6}O_x$ has the largest specific surface area (115.80 m^2/g) and the largest pore volume (0.27 cm^3/g). The excellent catalytic performance of $Mn_2Ce_1Cu_{0.6}O_x$ can be explained in terms of the rich pore structures, as bigger specific surface area and pore volume improved the diffusion and adsorption of organic contaminants [33]. Furthermore, all catalysts exhibited a unimodal pore size distribution centered around 3 nm, which facilitated the free diffusion of CVOCs molecules (0.5–1 nm) within the pores. This pore structure also supported the deposition of degradation products, enhancing catalytic activity [34]. In summary, Cu doping not only facilitated the formation of Cu-Mn solid solutions but also improved the textural properties, including specific surface area and pore volume, thereby enhancing catalytic performance.

The XRD patterns of catalytic fibers were shown in Fig. 4c. The diffraction peak at 18.1° corresponds to (100) planes of PTFE. As the Cu content increased, the intensity of this peak gradually diminished, suggesting a decrease in the crystallinity of catalytic fibers. To further evaluate the effect of catalyst content on the mechanical properties of PTFE fibers, the breaking force and elongation at break were measured as shown in Fig. 4d and 4e. Upon the addition of 20 wt% catalyst to the PTFE resin, the breaking force and elongation at break of fibers decreased significantly from 109.2 cN/dtex and 370 % to 73 cN/dtex and 260 %, respectively. Notably, 30C-PTFE showed similar mechanical properties with 20C-PTFE. However, when the catalyst content was further increased to 40 wt%, the mechanical properties of 40C-PTFE were sharply reduced and easy to break during stretching, which was not conducive to industrial production. Shore hardness of C-PTFE was measured on the 2 mm thick PTFE films and the results were shown in Fig. 4f. The hardness of C-PTFE increased with the increase of catalyst content from 25 HA (pure PTFE) to 60 HA (40C-PTFE), which was mainly attributed to intrinsic hardness of the catalyst particles. From the

perspective of industrial production, lower breaking force and elongation at break would cause film fracture in the production process and result in a lower yield. Excessive hardness could damage the extruder and calender, leading to the formation of uneven films. Conversely, poor mechanical properties would result in coarse fiber diameters and catalyst deactivation due to poor embedding within the fibers. Therefore, to balance mechanical performance and catalytic efficiency, the catalyst content should be controlled to a maximum of 30 wt%.

According to the TG curves (Fig. 4g), the total weight losses for pure PTFE, 20C-PTFE, 30C-PTFE, 40C-PTFE were 100 %, 81 %, 70 %, 60 %, respectively. There was no catalysts loss occurred during the preparation, which further confirmed that the decrease of catalytic activity of C-PTFE was caused by the encapsulation of catalysts within the fibers. C-PTFE exhibited excellent thermal stability as the pyrolysis of catalytic fibers occurred at 536 °C. To explore the hydrophobicity of C-PTFE, water contact angles were tested as shown in Fig. 4h and 4i. The water contact angles of pure PTFE (130.17°) and 40C-PTFE (129.49°) were both higher than 90°, indicating that 40C-PTFE inherited the excellent hydrophobicity of pure PTFE. Since flue gas from incineration process typically contains high humidity, strong hydrophobicity is beneficial for isolating catalysts from condensate water to avoid plugging the pore structures of catalyst.

3.4. Redox properties and acid sites

The redox properties of all catalysts were analyzed by XPS, O_2-TPD, and H_2-TPR. The O 1s, Mn 2p, Ce 3d and Cu 2p spectra were shown in Fig. 5a–d and the elemental valence state ratios were calculated based on the peak areas (Fig. 5e). The O 1s spectrum (Fig. 5a) could be deconvoluted into surface lattice oxygen (O_{latt}, 529.5 eV–530.0 eV) and surface chemisorbed oxygen (O_{ads}, 531.0 eV) [35]. The mobility of O_{ads} was higher than that of O_{latt} and O_{ads} was able to donate electrons more quickly in the reaction [36]. $Mn_2Ce_1Cu_{0.6}O_x$ had the highest content of O_{ads} (52.34 %), followed by $Mn_2Ce_1Cu_{0.2}O_x$ (50.34 %), $Mn_2Ce_1Cu_1O_x$ (48.26 %) and $Mn_2Ce_1O_x$ (43.58 %), which was consistent with the catalytic performance. It can be inferred that Cu doping contributed to the catalytic activity by increasing the proportion of O_{ads} content on the catalyst surface. The Mn $2p_{3/2}$ peak (Fig. 5b) can be deconvoluted into Mn^{2+} (640.5 eV), Mn^{3+} (642.2 eV) and Mn^{4+} (644.7 eV) [37]. Among them, Mn^{3+} was proposed to be the most active species for low-temperature CB oxidation [38]. The increase of Mn^{4+} content in $Mn_2Ce_1Cu_{0.6}O_x$ explained the excellent catalytic performance by

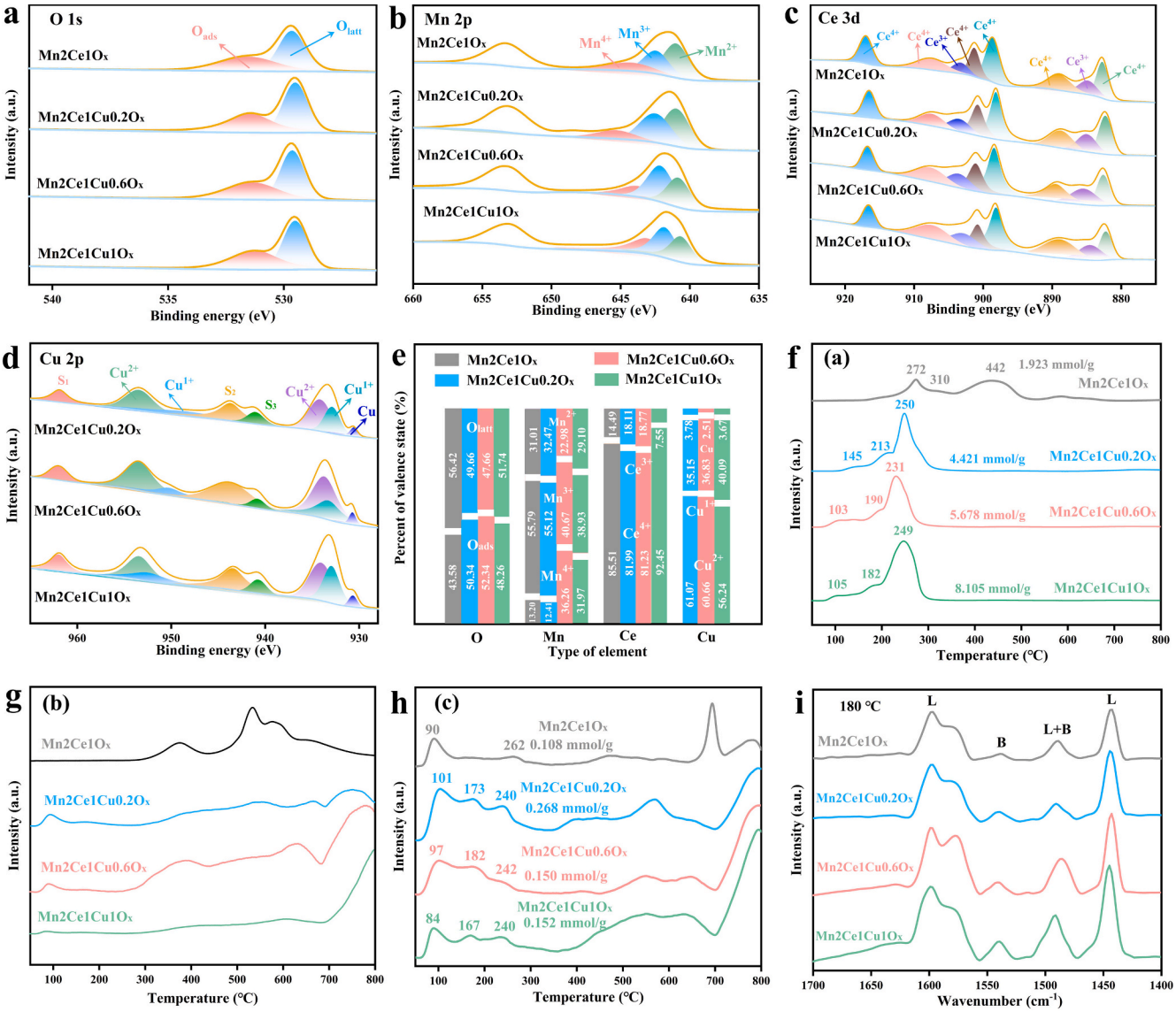

Fig. 5. XPS spectra of samples: O 1s (a), Mn 2p (b), Ce 3d (c) and Cu 2p (d); the percent of valence state (e), H_2-TPR (f), O_2-TPD (g), NH_3-TPD (h), Py-IR (i) of samples.

accelerating the oxidation of NO to NO_2 to facilitate the fast-SCR and CB oxidation [36]. The Ce 3d spectrum (Fig. 5c) was deconvoluted into eight peaks corresponding to Ce^{3+} and Ce^{4+}. The presence of Ce^{3+} proved the formation of oxygen vacancies and unsaturated chemical bonds due to charge imbalance on the surface of catalyst [39]. The Cu 2p peak (Fig. 5d) was divided into three peaks at 962.0, 943.7 and 940.8 eV belonging to Cu^{2+}, Cu^{1+} and metal Cu [40]. Three obvious satellite peaks at 962.0、943.7 and 940.8 eV represented the surface Cu^{2+} species. Cu^{2+} content was an important factor affecting redox reactions due to its strong oxidation capacity [23]. In addition, the coexistence of Ce^{3+} and Cu^{2+} can lower the redox potential and promote the formation of Cu-Ce solid solution [41]. To further verify the effect of Cu doping on the stability of catalysts, XPS analysis were performed on the catalyst before and after the stability test (Fig. S6). Interestingly, the O_{ads} content increased significantly after reaction from 47.66 % to 80.61 %, while Cu^{2+} content increased from 60.66 % to 72.92 %. Thus, the improving of Cu doping on the stability of catalysts can be attributed to that Cu^{1+} and mental Cu were oxidized during the reaction process and produced more O_{ads} on the catalyst surface [42]. O_{latt} on the surface of catalyst participated in the reaction, which proved that the synergistic removal reaction of CB and NO was consistent with the Mars-van Krevelen mechanism. Mn^{2+} content increased from 22.98 % to 31.97 % and Ce^{3+} content increased from 18.77 % to 24.90 % after 24 h reaction, indicating that there was not only the electron transfer between Mn and Ce, but also Ce and Cu. The Cl 2p spectrum (Fig. S6e) can be divided into peaks at 198.2 and 199.8 eV, corresponding to metal chlorides and organochlorine species, respectively. The peak at 206.6 eV represented the products of CB degradation or chloric acid or hypochlorous acid, which might come from residues in the solvent. Metal chlorides and organochlorine appeared on the surface catalyst indicated that Cl deposition happened during the reaction, leading to catalyst poisoning [43].

The synergistic removal of CB and NO was closely related to the reducibility of the catalyst. Therefore, the reducibility of all samples was analyzed by H_2-TPR and displayed in Fig. 5f. The reduction peaks can be attributed to the sequential reduction of $Mn^{4+}\rightarrow Mn^{3+}\rightarrow Mn^{2+}$ and $Cu^{2+}\rightarrow Cu^{1+}$. The hydrogen consumption of catalysts increased with the increase of Cu content in the following order: $Mn_2Ce_1Cu_1O_x$ (8.105 mmol/g) > $Mn_2Ce_1Cu_{0.6}O_x$ (5.678 mmol/g) > $Mn_2Ce_1Cu_{0.2}O_x$ (4.421 mmol/g) > $Mn_2Ce_1O_x$ (1.923 mmol/g), indicating that Cu doping greatly significantly enhanced the reducibility of the catalysts. Additionally, the reduction peak at 442 ℃ disappeared upon Cu doping, which is likely due to the weakened Mn-O bond energy caused by the incorporation of Cu [20]. Furthermore, O_2-TPD analysis was conducted to inestigate the surface oxygen species of all samples. Typically, the O_2-TPD spectra can be divided into three regions: low-temperature region (below 200 °C), middle-temperature region (200–400 °C) and high-temperature region (>400 °C) [44], corresponding to surface adsorbed oxygen, surface lattice oxygen, and internal lattice oxygen, respectively. It was observed that $MnCeCuO_x$ catalysts possessed more active oxygen species at low temperature, which were more prone to migration and participation in reactions. It can be inferred that Cu doping increased the content of surface adsorbed oxygen and promoted its migration.

The surface acidity of catalyst played a crucial role in the catalytic process. Fig. 5h displayed NH_3-TPD curves of $MnCeCuO_x$ catalysts and were divided into three distinct peaks corresponding to weak acid sites (100–200 °C), moderate acid sites (200–500 °C) and strong acid sites (500–700 °C) [45]. New peaks corresponding to weak and moderate acid site appeared on the Cu doping catalyst. The NH_3 desorption peak of $MnCeCuO_x$ catalysts also shifted to lower temperature compared to $Mn_2Ce_1O_x$. It can be inferred that Cu doping significantly increased acidic sites of catalyst according to the above analysis. To further investigate the surface acidity of samples, Py-IR was employed to identify the types and relative acidity of acid sites (Fig. 5i). The vibrational peak at 1542 cm^{-1} was attributed to Brønsted acid sites, while the peaks at 1450 cm^{-1} and 1606 cm^{-1} were attributed to Lewis acid sites. A peak at 1490 cm^{-1} was observed which was attributed to a synergistic peak of Lewis and Brønsted acid sites [42]. Quantification analysis of acid sites (Table. S4) revealed that Lewis acid sites were predominant on the surface of all samples. The acidity increased with the increase of Cu content, further proved that Cu doping promoted the generation of surface acid sites, especially Lewis acid sites. It was suggested that Brønsted acid sites were conducive to the adsorption of CB and Lewis acid sites were conducive to the break of C-Cl bond [46]. Therefore, we suggested that Cu doping improved the catalyst stability by promoting the complete oxidation of CB and reducing the chlorine poisoning. On the other hand, abundant H^+ helped improving the selectivity of HCl.

3.5. Catalytic mechanism

The synergistic catalytic mechanism of CB and NO over $Mn_2Ce_1Cu_{0.6}O_x$ was analyzed using in-situ DRIFTS experiments. As shown in Fig. 6a, the bands at 1029 and 1200 cm^{-1} were attributed to the bending vibration of the N—H of NH_3 coordinated at the Lewis acid sites [47], which was consumed after heating up to 250 °C. The peaks at 1367 and 1424 corresponded to $–NH_2$ and NH_4^+ species coordinated at Brønsted acid sites [48]. And the peak at 1546 cm^{-1} was attributed to the didentate nitrate [49]. The intensity of three peaks above increased significantly at 150 °C and then decreased at 250 °C, suggesting that adsorbed NH_3 reacted with oxygen to form $–NH_2$, NH_4^+ and nitrate. When the temperature rose to 250 °C, new peaks appeared at 1280 and 1600 cm^{-1} were associated with monodentate nitrate and bidentate nitrate, respectively. In-situ DRIFTS spectroscopy of CB catalytic oxidation was shown in Fig. 6b. The weak peak at 1086 cm^{-1} and 1380 cm^{-1} correspond to the tensile vibration of O—H in the alkoxide [50] and the C—O tensile vibrations in maleate, respectively [51]. The peak at 1564 cm^{-1} correspond to the tensile vibration of the surface acetate due to the destruction and oxidation of the aromatic ring [52]. Peaks of maleate and acetate increased at 150 °C and significantly decreased at 250 °C, indicating that both maleate and acetate were intermediates in the reaction, especially acetate. A new peak appeared at 1428 cm^{-1} at 150 °C suggested the formation of maleic anhydride [53]. The peak at 1652 cm^{-1} (CB adsorption) disappeared after heating up proved that CB adsorption was the first step of oxidation reaction. Peak at 2356 cm^{-1} was associated with asymmetric stretching vibration of C═O and adsorption of CO_2. When NO coexisted with CB (Fig. 6c), the peak intensity of NH_4^+ decreased slightly compared with Fig. 6a, which suggested that NH_4^+ was not consumed at 250 °C. Combined with the XPS results, we suggested that NH_4Cl was formed. The peak intensity of acetate decreased a lot at 150 °C compared with Fig. 6b, suggesting that CB oxidation was improved during synergistic removal reaction. The CO_2 absorption peak increased significantly at 250 °C, indicating that Cu doping improved the CO_2 selectivity of catalyst.

To verify the effect of Cu doping on the catalytic mechanism, same tests were performed on $Mn_2Ce_1O_x$ samples and in situ DRIFTS spectrum of two catalysts were compared as shown in Fig. 6d–i. Nitrogen-oxide significant peak was observed in Fig. 6d, indicating that both catalysts had excellent degradation effects on NO. The peak intensity of CB adsorption decreased after Cu doping (Fig. 6e). It was most likely that the increased acid sites after Cu doping promoted the reaction of adsorbed CB. As shown in spectrum over $Mn_2Ce_1O_x$ (Fig. 6f), the peak intensity of NH_4^+ increased greatly and the peak intensity of acetate decreased. But both peaks over $Mn_2Ce_1Cu_{0.6}O_x$ remained very weak. The NH_3-SCR reaction is inhibited by CB, which reacts with intermediates of strong oxidizing property (like NO, $–NH_2$ and so on), and remaining NH_4^+ reacted with the dissociated Cl^- to form sediment like NH_4Cl. Cu doping promoted the consumption of NH_4^+ to reduce the formation of NH_4Cl, which might explain the excellent stability of $Mn_2Ce_1Cu_{0.6}O_x$. On the other hand, intermediates of CB oxidation like carboxylate groups were quickly removed by reacting with amino groups like $–NH_2$ to reduce chlorine accumulation. Heating up to 250 °C, two curves of NH_3-SCR reaction were similar (Fig. 6g) but that of CB

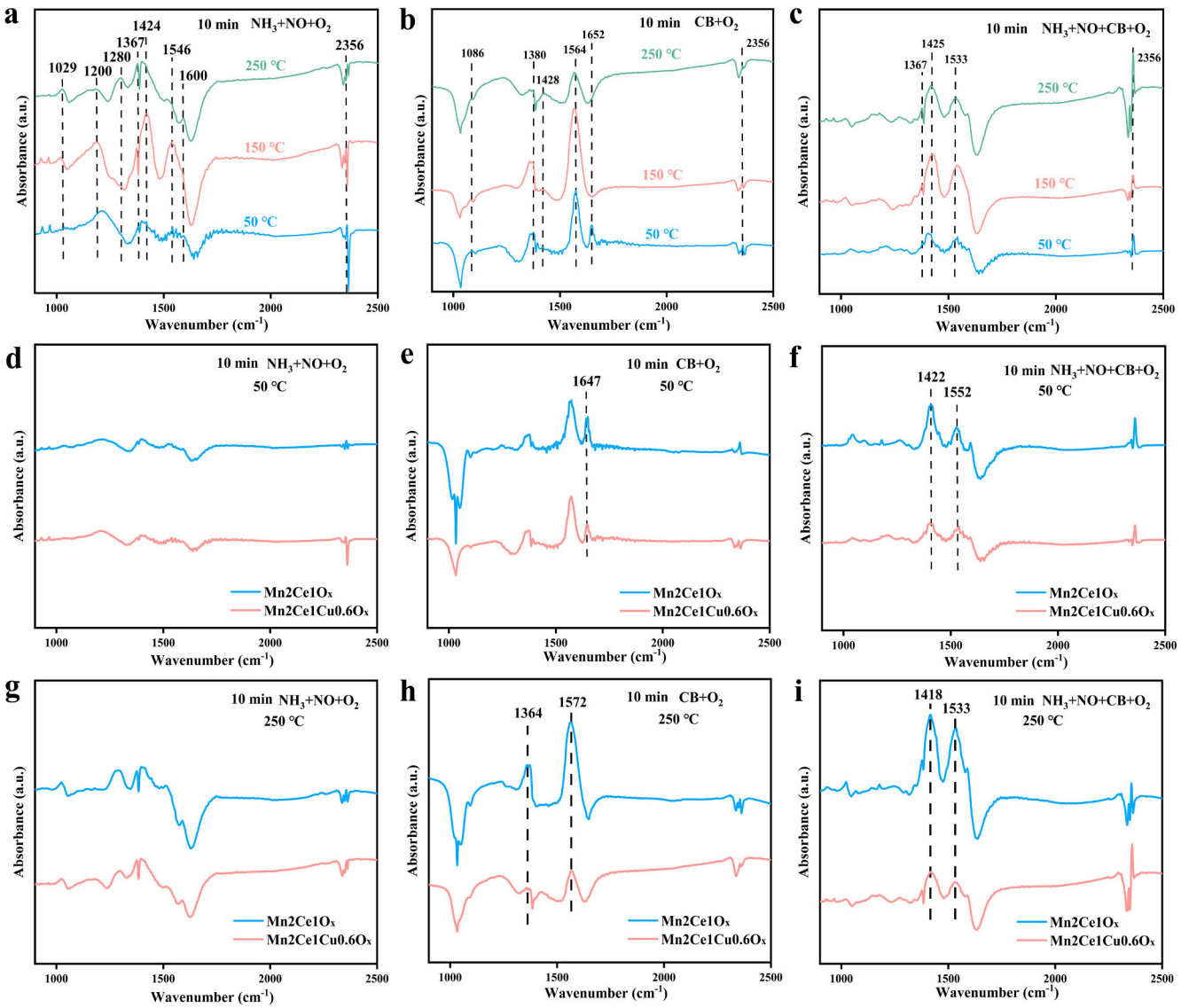

Fig. 6. In situ DRIFTS analysis on $Mn_2Ce_1Cu_{0.6}O_x$ under exposure to NO (a), CB (b), NO and CB (c) at different temperatures; in situ DRIFTS analysis on different catalysts at 50 ℃ (d–f) and 250 ℃ (g–i).

oxidation had a great difference (Fig. 6h). The decline of acetate peak intensity proved that Cu doping promoted the CB oxidation. The metallic sites presented on the Lewis acid metal sites can contribute to the CB oxidation by generating oxygen-metal adducts, promoting activation of reactive sites and subsequently facilitating the ring-opening process [54,55].

Based on the analysis above, a reaction mechanism for the synergistic removal of CB and NO was proposed. Ammonia (NH_3) was first coordinated at Lewis acid sites and reacted with NO and O_2 to form intermediate products (NH_4^+, $-NH_2$ and so on) and by-products (monodentate nitrate, bidentate nitrate and so on). Finally, NO was converted to N_2 and H_2O. On the other hand, CB was first adsorbed on the surface of catalyst to form a chlorinated intermediate, and then the C-Cl bond was dissociated and the benzene ring was opened to form major intermediates such as maleate and acetate. Finally, these intermediates were further oxidized to produce CO_2 and H_2O. During the synergistic removal reaction, NH_3-SCR reaction took precedence over CB oxidation to form intermediates with strong oxidizing properties. Then CB reacted with them rather than NH_4^+ to form acetates. Remaining NH_4^+ reacted with the dissociated Cl^- to form sediment like NH_4Cl and resulted in catalyst inactivation. Cu doping increased the Lewis acid sites, enhancing CB oxidation by improving CB adsorption and promoting benzene ring opening. This accelerated the reaction rate and electron cycling, which inhibited NH_4Cl formation, reduced chlorine deposition, and ultimately improved catalyst stability.

4. Conclusion

This study developed Cu-doped MnCeCuOx catalysts and catalyst-embedded PTFE fibers for the synergistic removal of CB and NO. Copper doping enhanced catalytic activity, with $Mn_2Ce_1Cu_{0.6}O_x$ achieving 90 % CB conversion and 100 % NO conversion at 180 °C. The 40C-PTFE fibers exhibited excellent CB catalytic performance (T_{90} = 185.4 °C). Dioxin removal experiments confirmed the catalysts' effectiveness. Cu doping improved catalytic activity primarily by increasing Lewis acid sites, forming solid solutions, enhancing pore structures, and increasing the presence of active oxygen species. As catalyst content increased, the mechanical properties of C-PTFE decreased, but catalytic activity improved. However, this enhancement was limited by the availability of catalyst loading sites, as catalysts embedded within the fibers did not contribute to the reaction. A catalyst content of 30 wt% was identified as optimal for C-PTFE preparation. Notably, C-PTFE also exhibited some

adsorption capacity for dioxins and SO_2, which could extend the service life of catalytic bag filters. During the synergistic removal process, the NH_3-SCR reaction took precedence over CB oxidation, forming strong oxidizing intermediates that reacted with CB. These intermediates facilitated the formation of acetates, while NH_4^+ reacted with Cl^- to form NH_4Cl, leading to catalyst deactivation. Cu doping enhanced CB oxidation by increasing adsorption and promoting benzene ring opening, accelerating reaction rates, and improving electron cycling. This inhibited NH_4Cl formation, reduced chlorine deposition, and improved catalyst stability. This study provides a cost-effective and eco-friendly strategy for the synergistic removal of multiple pollutants from flue gas.

CRediT authorship contribution statement

Shengyong Lu: Supervision, Funding acquisition, Conceptualization. **Xuanhao Guo:** Writing – original draft, Formal analysis, Data curation. **Manting Chen:** Writing – review & editing. **Guanjie Wang:** Funding acquisition, Formal analysis. **Juan Qiu:** Funding acquisition. **Jiaming Ding:** Formal analysis. **Minghui Tang:** Formal analysis. **Zhengdong Han:** Writing – review & editing. **Yaqi Peng:** Writing – review & editing, Funding acquisition. **Jianhua Yan:** Validation, Supervision.

Declaration of competing interest

The authors declare that they have no known competing financial interests or personal relationships that could have appeared to influence the work reported in this paper.

Acknowledgments

This work was supported by the National Natural Science Foundation of China (52206176), “Pioneer” and “Leading Goose” R&D Program of Zhejiang (2023C03125), Zhejiang Provincial Natural Science Foundation of China (LQ23E060002), Zhejiang Provincial Postdoctoral Research funding project (ZJ2024106) and Taizhou Science and Technology Plan Project (24sfa02).

Appendix A. Supplementary data

Supplementary data to this article can be found online at https://doi.org/10.1016/j.jcis.2025.137955.

Data availability

No data was used for the research described in the article.

References

[1] J. Cui, J. Li, H. Zhang, R. Zhang, W. Ma, Y. Zhu, W. Yuan, M. Palocz-Andresen, Y. Zhao, Z. Lou, Synergistic control potential of flue gas pollutants under Ultra-Low emission standards in waste incineration plants, Environ. Int. 186 (2024) 108590, https://doi.org/10.1016/j.envint.2024.108590.

[2] J. Qiu, Y. Peng, M. Tang, S. Lu, X. Li, J. Yan, Solvothermal preparation of Mn-based catalysts for simultaneous removal of 1,2-dichlorobenzene and furan, Waste Dispos. Sustain Energy 4 (2022) 105–116, https://doi.org/10.1007/s42768-022-00096-1.

[3] J. Qiu, M. Tang, Y. Peng, X. Guo, S. Lu, J. Yan, Simultaneous removal of 1,2-dichlorobenzene and furan over Mn–Ce–Fe oxide catalyst: Catalytic activity and product analysis, J. Rare Earths 42 (2024) 972–979, https://doi.org/10.1016/j.jre.2023.12.004.

[4] C. Zhang, J. Zhang, Y. Shen, J. He, W. Qu, J. Deng, L. Han, A. Chen, D. Zhang, Synergistic catalytic elimination of NO x and chlorinated organics: cooperation of acid sites, Environ. Sci. Technol. 56 (2022) 3719–3728, https://doi.org/10.1021/acs.est.1c08009.

[5] D. Kang, Q. Shi, C. Zhang, P. Zhao, H. Lyu, M. Yang, Y. Bian, B. Shen, Synergistic removal of NOx and CB by Co-MnOx catalysts in a low-temperature window, Chem. Eng. J. 476 (2023) 146369, https://doi.org/10.1016/j.cej.2023.146369.

[6] Y. Zhang, X. Wang, Y. Mao, C. Song, Z. Zhang, W. Zheng, Revealing the reaction regularity of Mn-CeO2-x catalyst system in catalytic filter for low-temperature NH3-SCR, J. Ind. Eng. Chem. 136 (2024) 222–228, https://doi.org/10.1016/j.jiec.2024.02.009.

[7] Z. Jiang, T. Cheng, Y. Hu, T. Liu, K. Qin, C. Zhu, Investigation of La-doped MnOx in PTFE filter bag for low-temperature selective catalytic reduction of NOx in cement industry flue gas with NH3, Mol. Catal. 556 (2024) 113940, https://doi.org/10.1016/j.mcat.2024.113940.

[8] R. Luo, Y. Zeng, S. Ju, S. Feng, F. Zhang, Z. Zhong, W. Xing, Flowerlike FeOX–MnOX amorphous oxides anchored on PTFE/PPS membrane for efficient dust filtration and low-temperature NO reduction, Ind. Eng. Chem. Res. 61 (2022) 5816–5824, https://doi.org/10.1021/acs.iecr.2c00272.

[9] Y. Peng, J. Ding, X. Guo, Q. Qiu, S. Lu, Y. Wang, B. Ma, Low-temperature catalytic oxidation of PCDD/Fs over MnCeCoOx/PPS catalytic filter, Environ. Sci. Pollut. Res. 30 (2023) 120355–120365, https://doi.org/10.1007/s11356-023-30768-2.

[10] J. Ho Boo, E. Kim, B. Chan Kwon, M. Jo Seo, J.-M. Kim, J. Bong Joo, D. Kang, N.-K. Park, Addition of V2O5-MnO2/USY-zeolite catalyst in PTFE fiber for bag filter and its catalytic activity tests for NH3-SCR at low-temperature, J. Ind. Eng. Chem. 123 (2023) 158–169, https://doi.org/10.1016/j.jiec.2023.03.032.

[11] Z. Chen, K.O. Kirlikovali, K.B. Idrees, M.C. Wasson, O.K. Farha, Porous materials for hydrogen storage, Chem 8 (2022) 693–716, https://doi.org/10.1016/j.chempr.2022.01.012.

[12] R. Zhang, L. Lu, Y. Chang, M. Liu, Gas sensing based on metal-organic frameworks: Concepts, functions, and developments, J. Hazard. Mater. 429 (2022) 128321, https://doi.org/10.1016/j.jhazmat.2022.128321.

[13] Y. Dai, C. Liu, Y. Bai, Q. Kong, H. Pang, Framework materials for supercapacitors, Nanotechnol. Rev. 11 (2022) 1005–1046, https://doi.org/10.1515/ntrev-2022-0042.

[14] H. Zhang, X. Hu, T. Li, Y. Zhang, H. Xu, Y. Sun, X. Gu, C. Gu, J. Luo, B. Gao, MIL series of metal organic frameworks (MOFs) as novel adsorbents for heavy metals in water: A review, J. Hazard. Mater. 429 (2022) 128271, https://doi.org/10.1016/j.jhazmat.2022.128271.

[15] X. Zhao, Z. Lu, Y. Zhang, M. Zhou, S. Xu, Z. Li, A review of recent progress in modified metal–organic frameworks as photocatalysts, J. Mater. Sci.: Mater. Electron. 33 (2022) 4737–4754, https://doi.org/10.1007/s10854-022-07717-9.

[16] M.S. Alhumaimess, Metal–organic frameworks and their catalytic applications, J. Saudi Chem. Soc. 24 (2020) 461–473, https://doi.org/10.1016/j.jscs.2020.04.002.

[17] S.-N. Zhao, X.-Z. Song, S.-Y. Song, H. Zhang, Highly efficient heterogeneous catalytic materials derived from metal-organic framework supports/precursors, Coord. Chem. Rev. 337 (2017) 80–96, https://doi.org/10.1016/j.ccr.2017.02.010.

[18] S. Chai, S. Li, W. Li, Q. Zheng, D. Wang, Y. Chen, Fabrication of high loading V2O5/TiO2 catalysts derived from metal-organic framework with excellent activity for chlorobenzene decomposition, Appl. Surf. Sci. 572 (2022) 151511, https://doi.org/10.1016/j.apsusc.2021.151511.

[19] T. Jiang, X. Wang, J. Zhang, Y. Mai, J. Chen, Highly efficient MnOx catalysts derived from Mn-MOFs for chlorobenzene oxidation: The influence of MOFs precursors, oxidant and doping of Ce metal, Mol. Catal. 551 (2023) 113653, https://doi.org/10.1016/j.mcat.2023.113653.

[20] J. Lei, J. Chen, B. Bai, P. Wang, S. Wang, J. Li, Regulation of the existing state of Cu species in high water-toletant CuOx-Mn3O4 for VOCs mixtrue catalytic oxidation, Chem. Eng. Sci. 284 (2024) 119455, https://doi.org/10.1016/j.ces.2023.119455.

[21] H. Ji, Y. Hou, B. Li, Y. Yang, S. Ma, Z. Huang, Insight into the mechanism of simultaneous removal of NOx and toluene by MnCuTi ternary catalyst, Mol. Catal. 559 (2024) 114110, https://doi.org/10.1016/j.mcat.2024.114110.

[22] C. Wu, G. Zhang, H. Zhao, M. He, H. Li, Z. Zhang, J. Ying, W. Zhou, The promotion mechanism of Mn on the catalytic degradation of benzene by H2O2 on Cu surface: The simultaneous enhancement of OH generation and benzene oxidation by ·OH, J. Environ. Chem. Eng. 12 (2024) 112438, https://doi.org/10.1016/j.jece.2024.112438.

[23] Q. Liu, M. Kashif, W. Deng, B. Zhao, P.M. Heynderickx, Y. Su, Exploring the role of Cu/Mn-BTC catalyst in the selective catalytic reduction of NOx by C3H6: Synthesis to in-situ DRIFTS study, Fuel 367 (2024) 131508, https://doi.org/10.1016/j.fuel.2024.131508.

[24] Y. Shen, J. Deng, L. Han, W. Ren, D. Zhang, Low-temperature combustion of toluene over Cu-doped SmMn2O5 mullite catalysts via creating highly active Cu2+–O–Mn4+ sites, Environ. Sci. Technol. 56 (2022) 10433–10441, https://doi.org/10.1021/acs.est.2c02866.

[25] F. Liu, J. Li, H.Y. Sohn, C. Chen, J. Yang, X. Liu, Y. Lan, W. Zhang, Q. Wang, L. Liu, Redox on Mn-Ce interface and its effects on low temperature selective catalytic reduction for NOx removal, Fuel 350 (2023) 128806, https://doi.org/10.1016/j.fuel.2023.128806.

[26] M. Chen, M. Yin, Y. Su, R. Li, K. Liu, Z. Wu, X. Weng, Atmospheric heterogeneous reaction of chlorobenzene on mineral α-Fe2O3 particulates: a chamber experiment study, Front. Environ. Sci. Eng. 17 (2023) 134, https://doi.org/10.1007/s11783-023-1734-9.

[27] P. Xu, Z. Jin, T. Zhang, X. Chen, M. Qiu, Y. Fan, Fabrication of a ceramic membrane with antifouling PTFE coating for gas-absorption desulfurization, Ind. Eng. Chem. Res. 60 (2021) 2492–2500, https://doi.org/10.1021/acs.iecr.1c00338.

[28] J. Wu, Y. Ying, Y. Ma, S. Zheng, X. Lin, X. Li, J. Yan, Influence of different loads on PCDD/F removal by SCR during municipal solid waste incineration, Chemosphere 338 (2023) 139516, https://doi.org/10.1016/j.chemosphere.2023.139516.

[29] B. Xie, Z. Wang, X. Zhang, M. Ding, M. Li, X. Guo, Q. Dai, L. Wang, W. Zhan, Y. Guo, A. Wang, Y. Guo, Morphology effect of cerium dioxide on the catalytic performance of Ru/CeO2 catalyst for the oxidation of different CVOCs, Sep. Purif. Technol. 345 (2024) 127428, https://doi.org/10.1016/j.seppur.2024.127428.

[30] J. Wan, F. Tao, Y. Shi, Z. Shi, Y. Liu, G. Wu, J. Kan, R. Zhou, Designed preparation of nano rod shaped CeO2-MnO catalysts with different Ce/Mn ratios and its highly

efficient catalytic performance for chlorobenzene complete oxidation: New insights into structure–activity correlations, Chem. Eng. J. 433 (2022) 133788, https://doi.org/10.1016/j.cej.2021.133788.
[31] Y. Yang, W. Si, Y. Peng, J. Chen, Y. Wang, D. Chen, Z. Tian, J. Wang, J. Li, Oxygen vacancy engineering on copper-manganese spinel surface for enhancing toluene catalytic combustion: A comparative study of acid treatment and alkali treatment, Appl. Catal. B 340 (2024) 123142, https://doi.org/10.1016/j.apcatb.2023.123142.
[32] C. Cocuzza, E. Sartoretti, C. Novara, F. Giorgis, S. Bensaid, N. Russo, D. Fino, M. Piumetti, Copper-manganese oxide catalysts prepared by solution combustion synthesis for total oxidation of VOCs, Catal. Today 423 (2023) 114292, https://doi.org/10.1016/j.cattod.2023.114292.
[33] R. Abazari, G. Salehi, A.R. Mahjoub, Ultrasound-assisted preparation of a nanostructured zinc(II) amine pillar metal-organic framework as a potential sorbent for 2,4-dichlorophenol adsorption from aqueous solution, Ultrason. Sonochem. 46 (2018) 59–67, https://doi.org/10.1016/j.ultsonch.2018.02.001.
[34] X. Shi, J. Guo, T. Shen, A. Fan, S. Yuan, J. Li, Enhancement of Ce doped La–Mn oxides for the selective catalytic reduction of NOx with NH3 and SO2 and/or H2O resistance, Chem. Eng. J. 421 (2021) 129995, https://doi.org/10.1016/j.cej.2021.129995.
[35] Z. Ye, J.-M. Giraudon, N. Nuns, G. Abdallah, A. Addad, R. Morent, N. De Geyter, J.-F. Lamonier, Preferential dissolution of copper from Cu-Mn oxides in strong acid medium: Effect of the starting binary oxide to get new efficient copper doped MnO2 catalysts in toluene oxidation, Appl. Surf. Sci. 537 (2021) 147993, https://doi.org/10.1016/j.apsusc.2020.147993.
[36] D. Kang, Q. Shi, C. Zhang, P. Zhao, H. Lyu, A. Huang, B. Shen, Modulation of acidic and redox properties of Mn-based catalysts by Co doping: Application to the synergistic removal of NOx and chlorinated organics, Sep. Purif. Technol. 339 (2024) 126695, https://doi.org/10.1016/j.seppur.2024.126695.
[37] T. Chen, R. Wang, C. Sun, D. Kong, S. Lu, X. Li, Metal-organic frameworks templated micropore-enriched defective MnCeOx for low temperature chlorobenzene oxidation, Appl. Catal. A 645 (2022) 118845, https://doi.org/10.1016/j.apcata.2022.118845.
[38] X. Weng, Q. Meng, J. Liu, W. Jiang, S. Pattisson, Z. Wu, Catalytic oxidation of chlorinated organics over lanthanide perovskites: effects of phosphoric acid etching and water vapor on chlorine desorption behavior, Environ. Sci. Technol. 53 (2019) 884–893, https://doi.org/10.1021/acs.est.8b04582.
[39] Y. Xia, Y. Yang, M. Li, Z. Lan, Y. Chu, G. Wu, D. Fang, Z. Zeng, H. Xiao, S. Deng, Y. Chen, Construction of unique oxygen vacancy defect through various metal-doping (Cu, Mn, Zr) of Ce2Co1Ox nanoparticles towards boosting the catalytic oxidation toluene performance, Sep. Purif. Technol. 342 (2024) 126993, https://doi.org/10.1016/j.seppur.2024.126993.
[40] J. Xiao, C. Zhang, L. Yang, S. Tang, W. Tang, Extraordinary synergy on 3D hierarchical porous Co-Cu nanocomposite for catalytic elimination of VOCs at low temperature and high space velocity, J. Environ. Sci. 151 (2025) 714–732, https://doi.org/10.1016/j.jes.2024.04.025.
[41] B. Song, C. Li, X. Du, S. Li, Y. Zhang, Y. Lyu, Q. Zhou, Superior performance of Cu-Ce binary oxides for toluene catalytic oxidation: Cu-Ce synergistic effect and reaction pathways, Fuel 306 (2021) 121654, https://doi.org/10.1016/j.fuel.2021.121654.
[42] Q. Zhang, S. Wu, L. Ding, N. Fang, H. Tang, Y. Chu, S. Ding, Acid-modified CoSnOx/MZSM-5 catalysts with the Cl poisoning resistance and high activity for catalytic oxidation of 1,2-dichloroethane, Sep. Purif. Technol. 339 (2024) 126619, https://doi.org/10.1016/j.seppur.2024.126619.
[43] P. Lu, L. Ye, X. Yan, J. Huang, Z. Tang, D. Chen, C. Cen, Poisoning mechanism of HCl over a Ru-based catalyst for toluene oxidation, Chem. Eng. J. 485 (2024) 149993, https://doi.org/10.1016/j.cej.2024.149993.
[44] X. Zhang, F. Bi, Z. Zhu, Y. Yang, S. Zhao, J. Chen, X. Lv, Y. Wang, J. Xu, N. Liu, The promoting effect of H2O on rod-like MnCeOx derived from MOFs for toluene oxidation: A combined experimental and theoretical investigation, Appl. Catal. B 297 (2021) 120393, https://doi.org/10.1016/j.apcatb.2021.120393.
[45] S. Chen, X. Li, L. Lin, X. Jing, W. Weng, Carbon template synthesis of CeO2 catalyst for direct conversion of methanol and carbon dioxide to dimethyl carbonate, J. Energy Inst. 107 (2023) 101190, https://doi.org/10.1016/j.joei.2023.101190.
[46] R. Gao, X. Tian, X. Ding, Z. Hou, Z. Li, X. Yu, J. Wang, L. Wu, L. Jing, J. Deng, Y. Liu, H. Dai, Regulating catalytic stability of PtSnM/CeO2 (M = Mn, W, Nb) catalysts via the closely coupled multi-active sites to promote multicomponent VOCs oxidation, Chem. Eng. J. 471 (2023) 144456, https://doi.org/10.1016/j.cej.2023.144456.
[47] P. Gong, J. Xie, D. Fang, F. He, F. Li, K. Qi, Enhancement of the NH3-SCR property of Ce-Zr-Ti by surface and structure modification with P, Appl. Surf. Sci. 505 (2020) 144641, https://doi.org/10.1016/j.apsusc.2019.144641.
[48] G. Li, Y. Zhang, P. Wu, K. Shen, S. Zhang, S. Ding, Improved activity and significant SO2 tolerance of Sb–Pd–V oxides on N-doped TiO2 for CB/NO synergistic degradation, Chemosphere 329 (2023) 138613, https://doi.org/10.1016/j.chemosphere.2023.138613.
[49] B. Lin, Z. Bao, A. Wang, Y. Ding, W. Zhan, L. Wang, Y. Guo, Q. Dai, Y. Guo, F. Gao, An efficient Co-Ni hydrous oxide catalyst for elimination of NO pollutant in semi-enclosed spaces at ambient temperature, Appl. Catal. B 337 (2023) 122984, https://doi.org/10.1016/j.apcatb.2023.122984.
[50] G. Hu, Z. Zhang, C. Wang, G. Li, D. Zhou, J. Wang, D. Che, R. Kang, New insight into oxygen vacancy and synergism in CuCeOx catalysts based on the toluene oxidation, J. Environ. Chem. Eng. 12 (2024) 112213, https://doi.org/10.1016/j.jece.2024.112213.
[51] H. Yang, A. Chen, F. Wang, T. Lan, J. Zhang, X. Hu, Y. Shen, D. Cheng, D. Zhang, Phosphotungstic acid as a dechlorination agent collaborates with CeO2 for synergistic catalytic elimination of NOx and chlorobenzene, Environ. Sci. Technol. (2024), https://doi.org/10.1021/acs.est.4c02246.
[52] M. Li, N. Wu, Q. Zhang, C. Gong, G. Xue, Synergistic removal of NOx and VOCs from flue gas on Mn-based catalysts, Catal Lett 154 (2024) 3516–3529, https://doi.org/10.1007/s10562-024-04585-2.
[53] L. Gan, P. Ye, X. Tian, J. Mi, J. Xing, Q. Xue, Q. Wu, J. Chen, J. Li, Simultaneous removal of NO and VOCs by Si doping CeO2 based catalysts: An acidity and redox properties balance strategy, Fuel 366 (2024) 131396, https://doi.org/10.1016/j.fuel.2024.131396.
[54] Y. Hu, R. Abazari, S. Sanati, M. Nadafan, C.L. Carpenter-Warren, A.M.Z. Slawin, Y. Zhou, A.M. Kirillov, A dual-purpose Ce(III)–Organic framework with amine groups and open metal sites: third-order nonlinear optical activity and catalytic CO2 fixation, ACS Appl. Mater. Interfaces 15 (2023) 37300–37311, https://doi.org/10.1021/acsami.3c04506.
[55] R. Abazari, S. Sanati, N. Li, J. Qian, Fluorinated metal–organic frameworks with dual-functionalized linkers to enhance photocatalytic H2 evolution and high water adsorption, Inorg. Chem. 62 (2023) 18680–18688, https://doi.org/10.1021/acs.inorgchem.3c03052.